Obrabotka metallov (tekhnologiya, oborudovanie, instrumenty) = Metal Working and Material Science. 2025 vol. 27 no. 2 pp. 43–56
ISSN: 1994-6309 (print) / 2541-819X (online)
DOI: 10.17212/1994-6309-2025-27.2-43-56

NSTU NETI

Obrabotka metallov - Metal Working and Material Science

Journal homepage: http://journals.nstu.ru/obrabotka_metallov

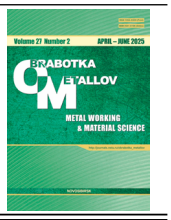

Microstructure and mechanical properties of Ti_2AlNb-based alloy weld joints as a function of gas tungsten arc welding parameters

Stanislav Naumov [1, a, *], ***Dmitrii Panov*** [1, b], ***Vitaly Sokolovsky*** [1, c], ***Ruslan Chernichenko*** [1, d], ***Gennady Salishchev*** [1, e], ***Dmitry Belinin*** [2, f], ***Vasilii Lukianov*** [3, g]

[1] Belgorod National Research University, 85 Pobedy Str., Belgorod, 308015, Russian Federation
[2] Perm National Research Polytechnic University, 29 Komsomolskiy Prosp., Perm, 614990, Russian Federation
[3] NPA "Technopark AT", 5 Tramvaynaya Str. (bld. 1), Ufa, 450027, Russian Federation

[a] https://orcid.org/0000-0002-4084-8861, NaumovStanislav@yandex.ru; [b] https://orcid.org/0000-0002-8971-1268, dimmak-panov@mail.ru;
[c] https://orcid.org/0000-0001-5607-2765, sokolovskiy@bsuedu.ru; [d] https://orcid.org/0000-0002-8619-0700, rus.chernichenko@mail.ru;
[e] https://orcid.org/0000-0002-0815-3525, salishchev_g@bsuedu.ru; [f] https://orcid.org/0000-0001-5462-0908, 5ly87@mail.ru;
[g] https://orcid.org/0009-0006-3621-3966, lukianovv@bk.ru

ARTICLE INFO

Article history:
Received: 12 February 2025
Revised: 01 March 2025
Accepted: 21 March 2025
Available online: 15 June 2025

Keywords:
Gas tungsten arc welding (*GTAW, TIG*)
Ti_2AlNb
Ti–Al–Nb–(Zr, Mo)–Si
Scanning electron microscopy (*SEM*)
Mechanical properties

Funding
This work was supported by the Russian Science Foundation (Agreement No. 19-79-30066) using the equipment of BSU Shared Research Facilities "Technologies and Materials".

ABSTRACT

Introduction. Gas tungsten arc welding (*GTAW*), also known as tungsten inert gas (*TIG*) welding, is a promising welding method for *Ti_2AlNb*-based alloys, including *Ti–Al–Nb–(Zr, Mo)–Si* alloy, due to its accessibility and relative simplicity, making it attractive for aerospace applications. However, the application of *GTAW* to *Ti–Al–Nb–(Zr, Mo)–Si* alloy is limited by the formation of a coarse-grained microstructure in the weld, leading to reduced mechanical properties of weld joints. **Purpose of the work.** This study investigates the influence of *GTAW* modes (using direct current with low- and high-frequency pulses) on the microstructure and tensile properties of *Al–Nb–(Zr, Mo)–Si* alloy weld joints. **Methods.** *GTAW* of plates was carried out using welding currents ranging from 80 to 150 A, employing both low- and high-frequency (>100 Hz) pulses. The microstructure of the weld joints was examined using scanning electron microscopy (SEM). The tensile properties were evaluated through uniaxial tensile testing of the welded joints. The shielding gas flow rate was 12 L/min, while a separate gas flow of 2 L/min was used for blowing. The microstructure of the weld joints was examined using scanning electron microscopy (*BSE-EBSD* analysis). The tensile properties were evaluated through uniaxial tensile testing of the weld joints. **Results and discussion.** The weld joints microstructure is characterized by elongated, coarse dendrites in the central and weld bead regions and globular β-grains in the root part of the fusion zone. Tensile testing of the weld joints revealed a strength level approximately 90% of that of the base metal when using pulse mode (σ_u = 1100 MPa, δ = 1.1 %, 335–390 $HV_{0.2}$) and not less than 80% when using direct current modes. This level of mechanical properties is achieved using high-frequency pulsed welding, where the maximum length and width of dendrites in the weld joint are 1.06 mm and 0.33 mm, respectively, and the average size of globular grains in the lower part of the weld joint is approximately 130 μm, which is less than that observed when utilizing the same modes, but direct current.

For citation: Naumov S.V., Panov D.O., Sokolovsky V.S., Chernichenko R.S., Salishchev G.A., Belinin D.S., Lukianov V.V. Microstructure and mechanical properties of Ti_2AlNb-based alloy weld joints as a function of gas tungsten arc welding parameters. *Obrabotka metallov (tekhnologiya, oborudovanie, instrumenty) = Metal Working and Material Science*, 2025, vol. 27, no. 2, pp. 43–56. DOI:10.17212/1994-6309-2025-27.2-43-56. (In Russian).

Introduction

Titanium alloys have found widespread application in various industries, including aerospace, mechanical engineering, medicine, and other fields, due to their low density, high strength, corrosion resistance, excellent manufacturability, and other beneficial properties [1–4]. However, the high-temperature applications of titanium alloys are limited by their creep and oxidation resistance up to 500–550 °C [5].

*** Corresponding author**
Naumov Stanislav V., Ph.D. (Engineering),
Belgorod National Research University,
85 Pobedy Str.,
308015, Belgorod, Russian Federation
Tel.: +7 912 580-55-68, **e-mail:** NaumovStanislav@yandex.ru

A potential solution to the problem of high-temperature service lies in intermetallic compounds and alloys [6]. Alloys based on the orthorhombic titanium intermetallic (ortho-*Ti_2AlNb* alloys) are promising materials in this regard. *Ti_2AlNb*-based alloys exhibit low density (5.1…5.4 g/cm^3), high specific strength, oxidation resistance, and creep resistance [7–10]. However, their practical application is complicated by difficulties in welding, which is one of the most significant limiting factors [11]. This is primarily due to the generation of high residual stresses resulting from a cascade of phase transformations in the fusion and heat-affected zones (*FZ*, *HAZ*) during welding, low thermal conductivity (6.2 W/(m·K) [10]) and low ductility of *Ti_2AlNb*-based alloys. Therefore, by varying welding parameters to control heat input, it is necessary to ensure the formation of an optimal weld structure and to create conditions for slow cooling of the weld metal to prevent cracking [12–14].

To address these issues, various specialized welding methods with supplementary techniques are employed, such as heating of the workpieces before and during welding (preheating and additional heating). Furthermore, heat treatment is used to improve mechanical properties [15–18]. Despite the wide variety of methods, techniques, and operations used in welding titanium alloys, gas tungsten arc welding (*GTAW, TIG* welding) remains the most promising for industrial applications, which is determined by the formation of defect-free welds and its wide availability. However, the formation of a coarse-grained structure and a wide weld region limits its application due to the low mechanical properties, namely ultimate tensile strength (σ_u) and percentage of elongation (δ), of the welded joints [19, 20].

Currently, leveraging the accumulated global experience in *GTAW* of titanium alloys, it is possible to enhance the mechanical properties of welded joints made from *Ti_2AlNb*-based alloy by employing *GTAW* with speed-up direct current and using low- and high-frequency pulsing. This allows for the regulation of the heat spot power and, consequently, the heat input into the workpiece, creating conditions to prevent the growth of dendritic structures in the weld metal [21]. Therefore, ***the purpose of this research*** is to investigate the influence of *GTAW* conditions on the microstructure and mechanical properties of welded joints made from *Ti_2AlNb*-based alloy. To achieve the set purpose, it is proposed to solve several problems. Namely, the first problem is to select *GTAW* weldig conditions using direct current and with the application of low- and high-frequency pulsing to obtain defect-free welded *Ti_2AlNb*-based alloy joints. Subsequent problems involve studying the microstructure, microhardness, and mechanical properties of the obtained welded joints compared to the properties of the base material.

Methods

The chemical composition of the initial *Ti_2AlNb*-based alloy is presented in Table 1. The hot-forged workpiece of the *Ti_2AlNb*-based alloy in the initial state exhibits the following properties: ultimate tensile strength (σ_u) = 1,230 MPa, offset yield strength ($\sigma_{0.2}$) = 1,190 MPa, percentage of elongation (δ) = 3.5 %, and microhardness = 400 ± 10 $HV_{0.2}$. The microstructure of the initial material (Fig. 1) consisted of large β-grains elongated perpendicular to the forging direction and 300 ± 50 μm in size. Furthermore, a globular α_2-particles (*Ti_3Al*) with a size of 10 ± 5 μm were located along the β-grain boundaries. Particles of the acicular O-phase (Ti_2AlNb) particles with a length of 8 ± 3 μm and a thickness of 1–3 μm were uniformly distributed throughout the entire volume of the material under study.

TIG welding was performed on *INVERTEC V405-T pulse* equipment (*Lincoln Electric*, USA) using a *WP-9 flex* welding torch (*Start*, Russia) and *WT-20* electrodes (*Start*, Russia). Argon was used as the shielding gas. Gas shielding was implemented using a 12 mm diameter gas lens at the welding site and

Table 1

Chemical composition of *Ti–Al–Nb–(Zr, Mo)–Si* alloy

Element	*Al*	*Nb*	*V*	*Zr*	*Mo*	*Si*	*Ti*
at. %	23.0	23.0	1.4	0.8	0.4	0.4	base

additional blowing into the weld root (Fig. 2, *a*). The shielding gas flow rate was 12 L/min, and the gas for blowing rate was 2 L/min.

The workpieces for *GTAW* (25×15×2 mm) were cut from the forged piece using *VL400Q* and *VL600Q* wire electrical discharge machines (*Sodick*, China). The surface of the workpieces was prepared before *GTAW* using abrasive paper: the abutting surfaces were ground with *FEPA P1000* (18 μm, GOST No. M20) abrasive paper, and the remaining surfaces were ground with *FEPA P220* (68 μm, GOST No. 6) abrasive paper. Welding of the 2 mm thick plate workpieces was performed in a butt joint configuration. Welding was performed using speed-up welding condition. Low- and high-frequency pulsed welding was also used in the study (Table 2). A feature of gas tungsten arc welding using low- and high-frequency pulsing is that additional pulses with a specified amplitude are superimposed on the effective constant welding current, forming energy peaks that exceed the background current. At the same time, the formation of the welds occurs sequentially in a droplet mode, which eliminates metal spatter and allows for the production of thin-walled welded joints without burn-through. Arc ignition was performed on the edge of the workpieces being welded due to the absence of runoff plates. The welding current range was 80…150 A.

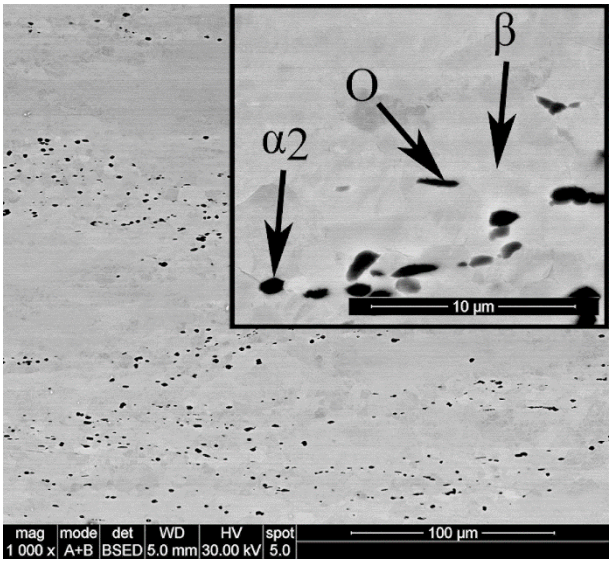

Fig. 1. Initial microstructure of the *Ti–Al–Nb–(Zr, Mo)–Si* alloy

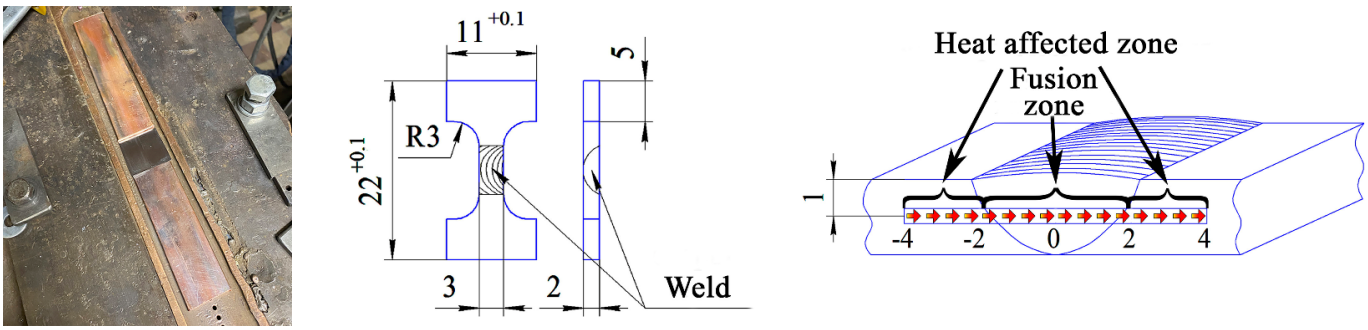

a *b* *c*

Fig. 2. GTAW welding fixture (*a*), specimens for mechanical testing (*b*) and microhardness testing specimens (*c*) of the welded joint of *Ti–Al–Nb–(Zr, Mo)–Si* alloy

Specimens for uniaxial tensile testing, microstructural analysis, and microhardness testing were ground with silicon carbide-based abrasive papers *FEPA P* 220–2000 (*Struers*, Denmark) on a grinding and polishing machine (*Chennai Metco BAINPOL*, India). The polishing was carried out on a 200 mm polishing wheel made of *MD-Nap* cloth from *Struers* using *O.P.S* (*MetCata*, Germany) or *OP-S* (*Struers*, Denmark) 0.05 μm suspension.

To determine the mechanical properties of the welded joints made of *Ti–Al–Nb–(Zr, Mo)–Si* alloy, uniaxial tensile tests were performed using a *5882* universal testing machine (*Instron*, USA). The test temperature corresponded to room temperature. The strain rate during tensile testing was set to 10^{-4} s^{-1}. The shape and dimensions of the uniaxial tensile test specimens are shown in Fig. 2.

The microhardness was measured in the cross-section of the welded joints using a *402MVD* microhardness tester (*Instron*, Netherlands) equipped with a diamond indenter. The load applied to the indenter corresponded to 200 g with a holding time of 10 sec. The distance between measurements was 100 μm. The measurement was carried out along one line in the center of the specimen, i.e., at a depth of 1 mm, as shown in Fig. 2, *c*.

The microstructure was evaluated using scanning electron microscopy (*BSE* and *EBSD* analysis), namely, evaluation of the presence of internal defects (pores, cracks, lack of fusion), identification of phases, and geometric dimensions of the microstructure elements in the weld metal and heat-affected zone (*HAZ*). *BSE* and *EBSD* analysis was performed using a *Q600 3D* instrument (*FEI*, Czech Republic) using *TSL OIM Analysis 9* software with a scanning step of 3 μm and an accelerating voltage of 30 kV.

Results and discussion

Fig. 3 shows the appearance of welded joints. The welded joints obtained in the selected modes (Table 2) do not have external cracks, pores or heat colors. The presence of defects at the beginning and end of the welds is attributed to the absence of run-off plates (Fig. 3). At currents of 80–85 A (mode No. 1), a fine scaling pattern is observed on the weld bead. A localized lack of fusion was found in the weld root, which could potentially be eliminated by a more uniform welding speed. In speed-up welding condition at ***I*** = 150…155 A (mode No. 2), burn-through of the plates occurred; furthermore, the liquid metal locally accumulated under the force of surface tension, forming a drop-shaped weld bead. Thus, burn-through occurred on part of the plate, while a wide weld formed on another part. This mode is not suitable for *GTAW* of *Ti–Al–Nb–(Zr, Mo)–Si* alloy plates 2 mm thick. At increased currents of 110…115 A (mode No. 3), defects did not form, ensuring a uniform, fine-ripple weld with full fusion of the plates (Fig. 3, *b*). However, the weld width (mode No. 3) is 1.5 times wider compared to mode No. 1, and the melting of the plate edges is more intense. On average, the weld width obtained with direct current was 5…8 mm.

Table 2

Modes of *GTAW* for *Ti–Al–Nb–(Zr, Mo)–Si* alloy plates

No.	Current, A	Pulse frequency, Hz	Shielding gas, L/min	Blowing L/min	Comments
1	80–85	–	12	2	local lack of fusion
2	150–155	–	12	2	burn-through
3	110–115	–	12	2	–
4	80–85	2	12	2	coarse scaling
5	80–85	>100	12	2	fine scaling
6	110–115	>100	15	2	fine scaling

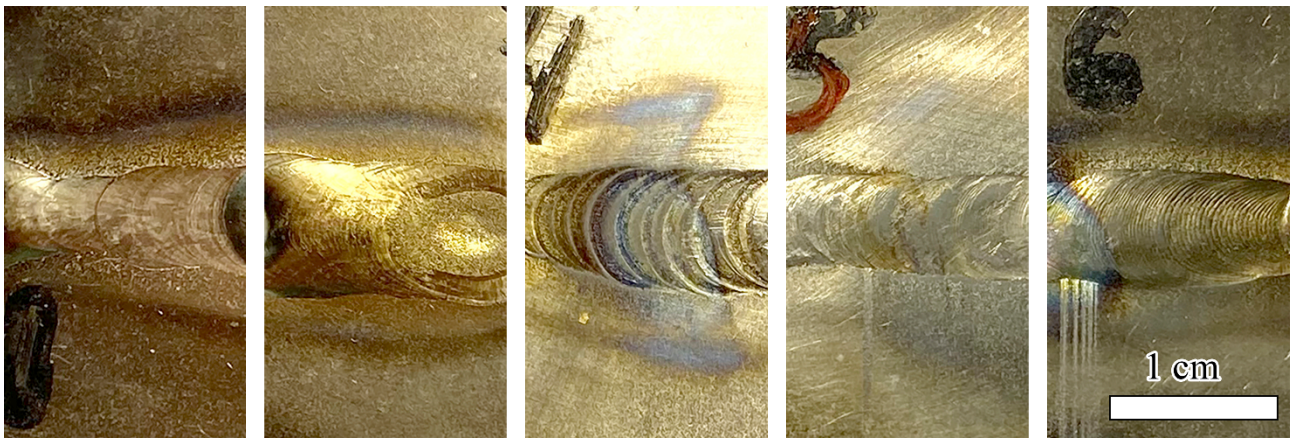

a *b* *c* *d* *e*

Fig. 3. Appearance of *Ti–Al–Nb–(Zr, Mo)–Si* alloy weld joints produced by *GTAW* under:
a – direct current (mode No. 1); *b* – direct current (mode No. 3); *c* – low-frequency pulse (mode No. 4); *d* – high-frequency pulse (mode No. 5); *e* – high-frequency pulse (mode No. 6)

During *GTAW* with a low-frequency pulse of 2 Hz at currents of 80–85 A (mode No. 4), a coarse scaling pattern formed on the surface of the weld bead under the dynamic effects of the pulsed current (Fig. 3, *c*). Since the effects of the pulsed current allows reducing the welding speed, it promotes more intensive fusion of the weld root at the same current values as in mode No. 1. Welded joints obtained in modes No. 5 and No. 6 were obtained using a high-frequency pulse of more than 100 Hz. These modes provided a fine scaling pattern on the surface of the weld bead; however, when the current is increased to 110…115 A, melting of the plate edges occurred. The weld width obtained with pulsed currents was 5…7 mm.

The reduction in the weld width can be explained by the influence of the welding current, namely, the effect of the pulsed current reduces the average power in the heat heating spot [22].

A typical morphology of the weld cross-section is shown in Fig. 4. In the upper part of the weld, a wide fusion zone (*FZ*) of the metal formed (Fig. 4, *a*) because of the action of the electric arc [23]. The weld metal consists entirely of β-grains (Fig. 4, *b*). The intense heating of the weld metal caused by the electric arc and, as a consequence, the wide weld (5–8 mm) also led to the formation of a wide *HAZ*. Depending on the phase composition, the *HAZ* can be divided into *HAZ1* and *HAZ2*. *HAZ1* consists of large β-phase grains 150 ± 50 μm (Fig. 4, *c*), whereas *HAZ2* consists of β (80 ± 30 μm) + α_2 (4 ± 2 μm) grains. It is known that with a greater distance from the fusion line, the phase composition in the *HAZ* (β+ α_2) also additionally contains the O-phase [24].

The weld metal formed at direct and pulsed currents possesses a microstructure in the form of columnar grains at the bead and globular grains in the root part of the weld (Fig. 5). Primary crystallization begins when heat is removed to the base material, originating along the *FL*. The primary crystallization of the weld metal proceeds periodically, and a layered structure can be found (Fig. 4, *a*). The main volume of the

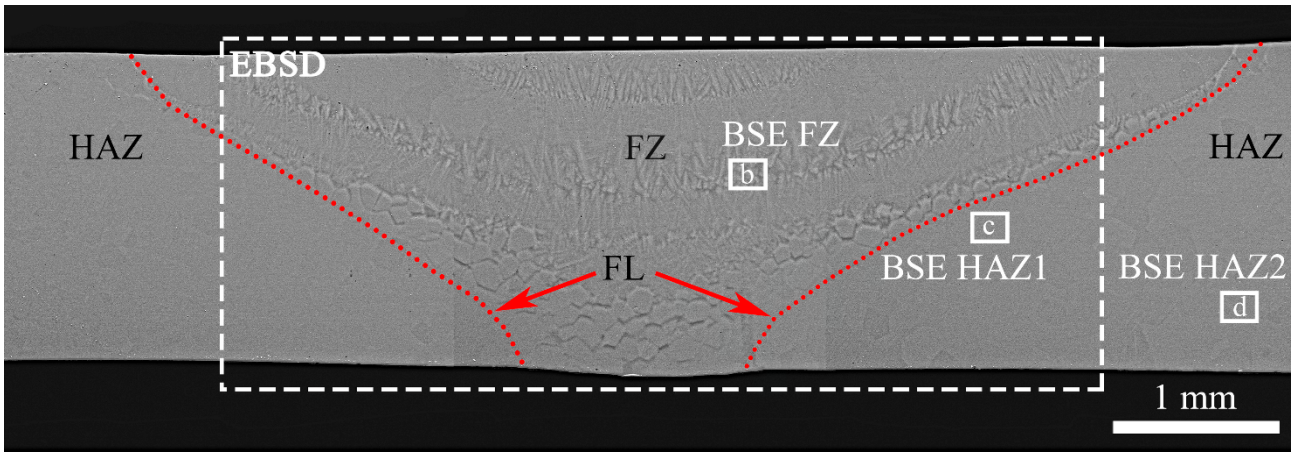

a

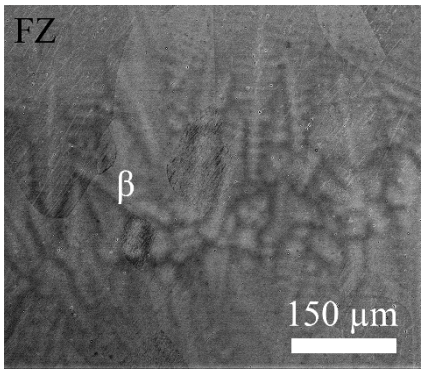

b

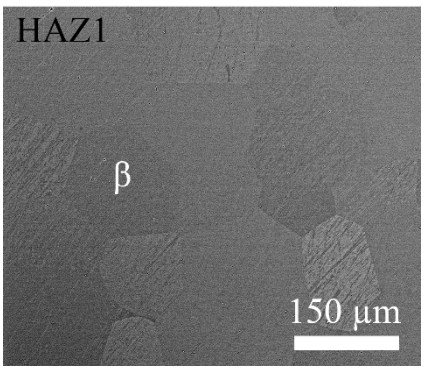

c

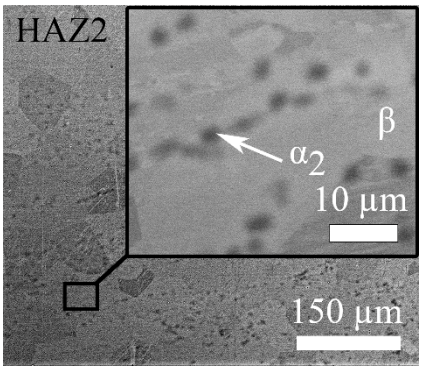

d

Fig. 4. BSE-analysis of a *Ti–Al–Nb–(Zr, Mo)–Si* alloy weld joint obtained by *GTAW* according to mode No.4:
a – general view showing the locations of *BSE* and *EBSD* analyses (*FL* – fusion line; *FZ* – fusion zone; *HAZ* – heat-affected zone); *b* – *FZ*; *c* – *HAZ* with coarse β-grains (*HAZ1*); *d* – *HAZ* with β + α_2 phase composition (*HAZ2*)

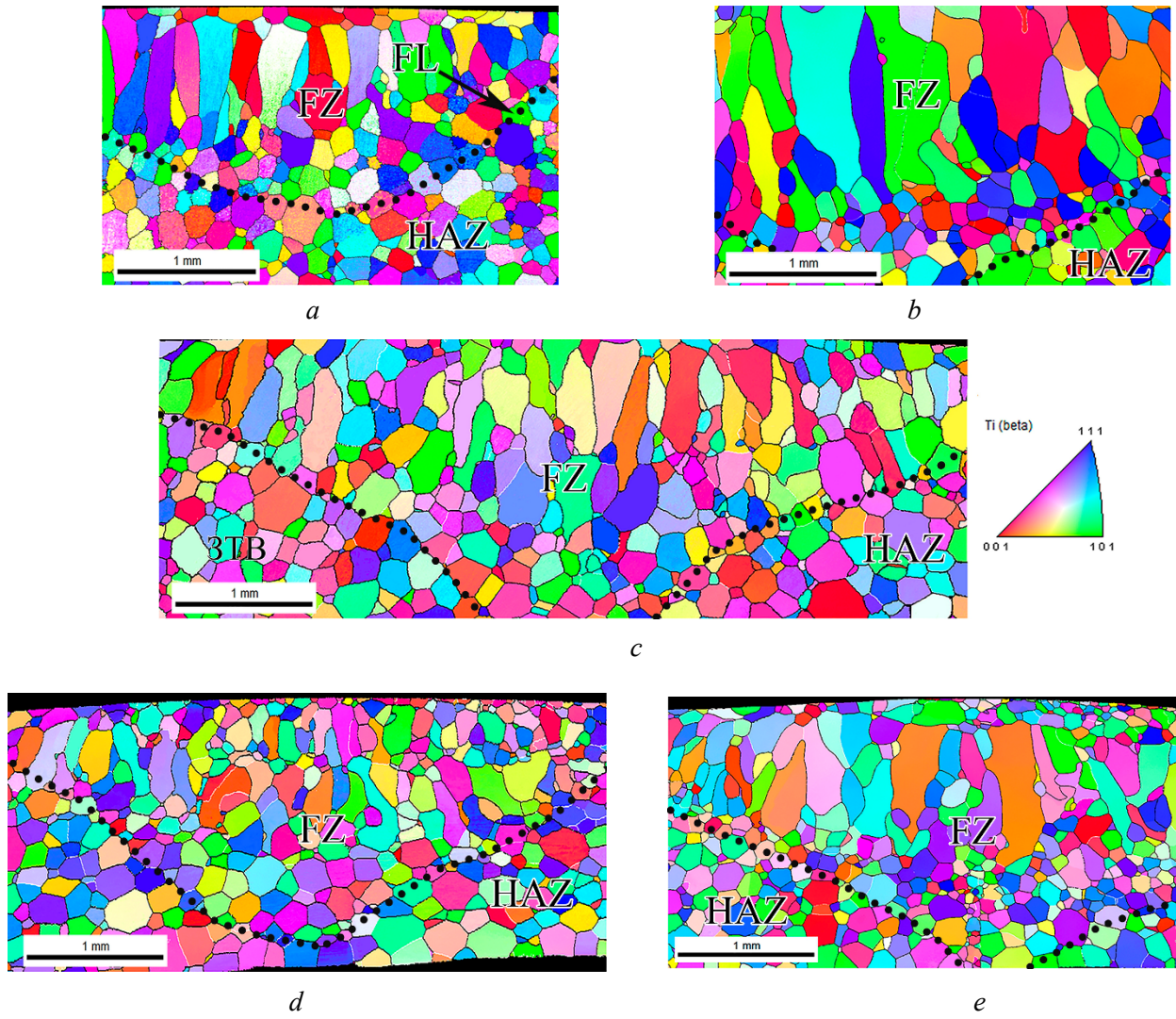

Fig. 5. EBSD maps in cross-section of *Ti–Al–Nb–(Zr, Mo)–Si* alloy weld joints, obtained by *GTAW* according to: *a* – mode No. 1; *b* – mode No. 3; *c* – mode No. 4; *d* – mode No. 5; *e* – mode No. 6

molten pool is concentrated in the immediate vicinity of the welding arc, so columnar dendrites formed in the central and upper part of the weld, where the maximum heat removal is observed.

The maximum length (L_{max}) and width (H_{max}) of dendrites in welds made at currents of 110–115 A is ≈ 1.39 mm and 0.43 mm (mode No. 3), with a decrease in current (mode No. 1), the L_{max} and H_{max} of dendrites are ≈ 0.99 mm and 0.23 mm, respectively (Table 3). With an increase in the welding current, the width of the zone with globular grains decreases; however, the average grain size does not change and remains within 140 ± 50 μm (Fig. 5, *a*, *b*). In welding mode No. 3, localized incomplete fusion (lack of fusion) is observed at the root of the weld (Fig. 5, *a*), which was confirmed previously during visual inspection of the weld appearance.

Table 3

Maximum dendrite length and width (L_{max}, H_{max}) and average globular grain size in the weld joint metal as a function of *GTAW* modes

Welding modes	No.1	No.2	No.3	No.4	No.5	No.6
L_{max} (mm)	0.99	–	1.39	0.98	0.61	1.06
H_{max} (mm)	0.23	–	0.43	0.27	0.23	0.33
Average globular grain size (μm)	140 ± 50	–	140 ± 50	190 ± 40	140 ± 40	130 ± 45

When welding in low-frequency pulsed modes, the *FZ* structure does not differ from the structure of welds obtained in modes No. 1 and No. 3. The L_{max} and H_{max} of dendrites in the weld, obtained in the low-frequency pulse mode (mode No. 4), are ≈ 0.98 mm and 0.27 mm, respectively, and the average size of the globular grains is ≈ 190 μm (Fig. 5, *c*). However, when using high-frequency pulsed current (mode No. 5), the L_{max} and H_{max} of dendrites in the weld decreases to ≈ 0.61 mm and 0.23 mm, and the average size of the globular grains is ≈ 140 μm (Fig. 5, *d*). In welding mode No. 5, a localized lack of fusion of 100…150 μm can be observed (Fig. 5, *d*), which is smaller than at the same welding current parameters in mode No. 1 (300…500 μm). With an increase in the high-frequency current values (mode No. 6), the L_{max} (1.06 mm) and H_{max} (0.33 mm) of the β-phase dendrites increases, while the average size of the globular β-grains in the lower part of the weld remains at ≈ 130 ± 45 μm (Fig. 5, *e*), which is smaller than at the same currents without the pulsed mode No. 3. The above results show that the pulsed welding current demonstrates periodic changes in the dynamic effects of the arc, which can enhance the effect of mixing the molten pool and thereby reduce the grain size in the weld [25].

The microhardness profile in the cross-section of welded joints obtained with direct current along the entire length is at the same level, since the weld width varies within 5…8 mm and the values correspond to the microhardness of the FZ and the *HAZ1* with globular β-phase grains (Fig. 6, *a*, *b*). The range of values varies from 335 to 390 $HV_{0.2}$. The range of microhardness values of welds obtained with pulsed currents is in the range of 340…380 $HV_{0.2}$ (Fig. 6, *c*, *d*, *e*).

Tensile tests of welded joints obtained *GTAW* (Fig. 7) showed that the strength level of the joints welded in mode No. 6 reaches ≈ 90 % of the base metal (σ_u = 1,100 MPa, δ = 1.1 %), and is not lower than 80 % of the base metal in modes No. 4 and No. 5 (σ_u = 1070 MPa, δ = 1.49 %) (Fig. 7, *a*). However, the ductility of the welded joint obtained in mode No. 5 is absent (σ_u = 960 MPa, δ = 0 %), and for the welded joints obtained in modes No. 4 and No. 6, it drops by 2–3 times in relation to the base metal and amounts to no more than 2 % (Fig. 7, *b*).

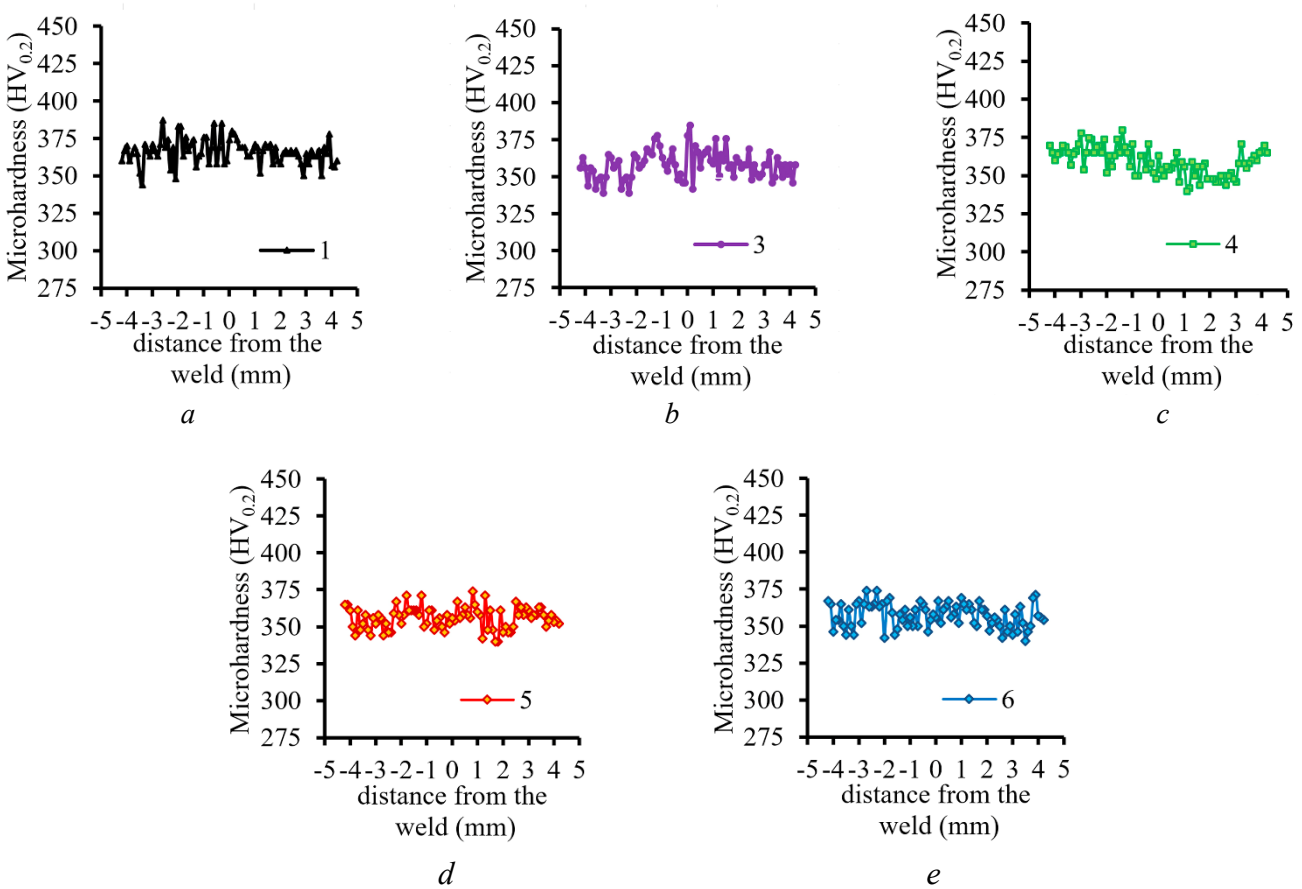

Fig. 6. Cross-sectional microhardness profiles of *Ti–Al–Nb–(Zr, Mo)–Si* alloy *GTAW* joints according to: *a, b – DC* mode*; c, d, e* – pulsed mode

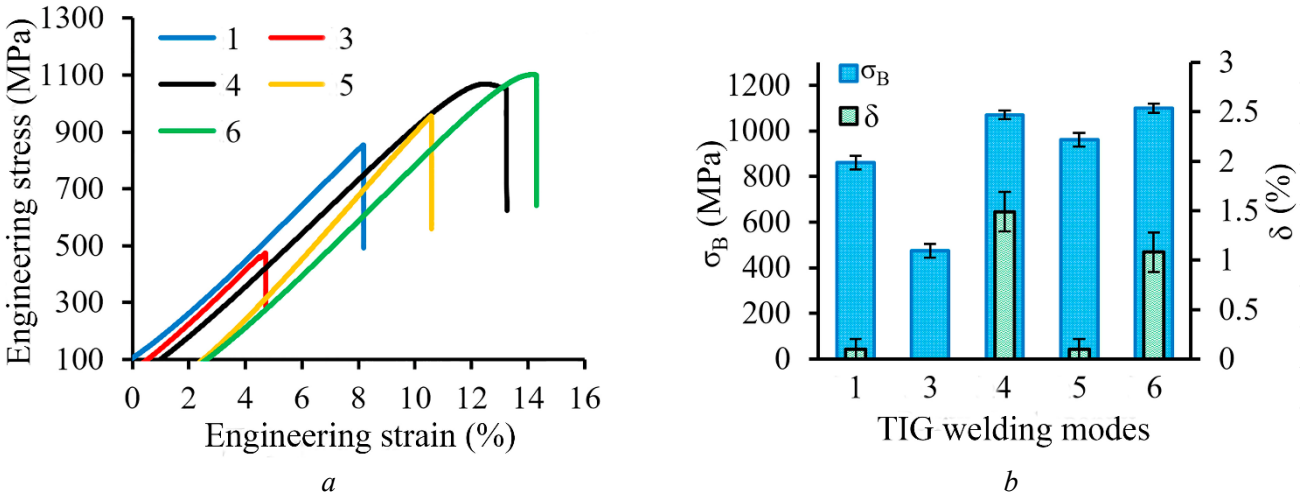

Fig. 7. Results of uniaxial tensile testing of *Ti–Al–Nb–(Zr, Mo)–Si* alloy weld joints as a function of *GTAW* modes:
a – tensile stress-strain diagram; *b* – graph of mechanical properties

In welded joints obtained with direct current welding, the joints perform extremely low ductility and strength properties. In welds obtained in mode No. 1, a localized lack of fusion was observed, which led to a decrease in strength to less than 80 %. In addition, the strength of the welded joint obtained in mode No. 3 is ≈ 40 % of the strength of the base metal. This is due to the fact that in this mode, the maximum grain size of the dendritic structure of the *FZ* was found, which exceeds by 1.5 times the maximum sizes of dendrites in the *FZ* of welded joints obtained with low- and high-frequency pulsed modes. When welding in mode No. 5, the decrease in the strength properties of the welded joint is possibly related to the localized lack of fusion that was found in the root part of the weld (Fig. 5, *d*).

Fracture of the welded joints always occurs along the fusion line, and a river line pattern is visible on the fracture surface, mainly caused by the fracture of large β-grains (Fig. 8). The fracture surface of the sample welded in mode No. 6 has 2 zones, namely: a fracture area of large (dendritic structure of the *FZ*) and small grains. The phenomenon indicates the fracture of globular β-grains, which were formed in the root area of the weld (Fig. 8). A similar fracture pattern is observed on the remaining samples.

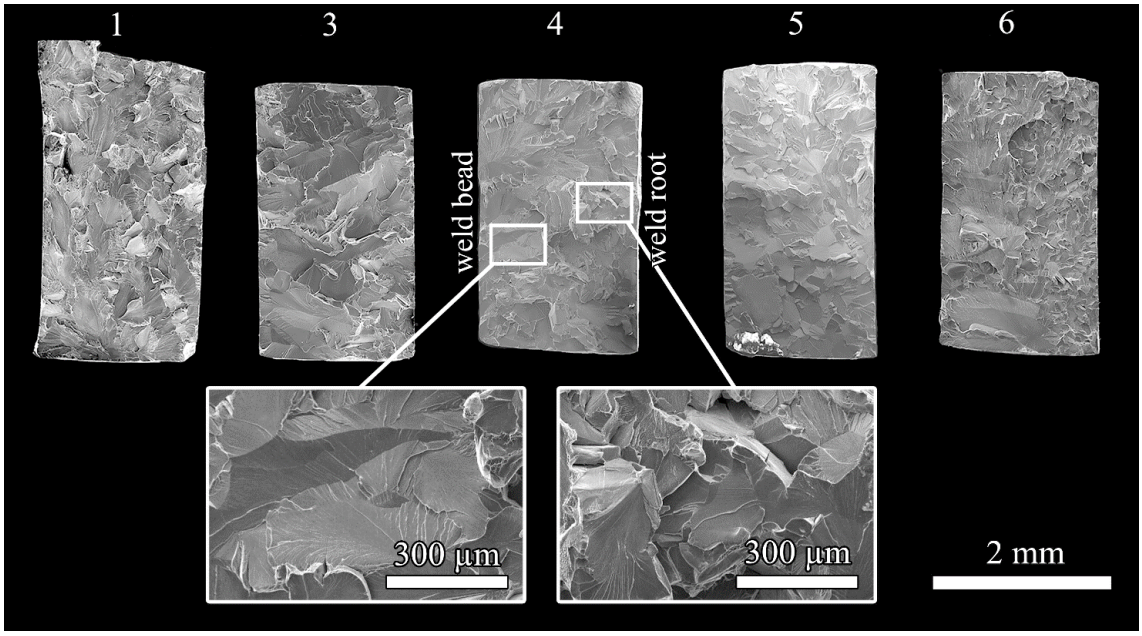

Fig. 8. Fracture surface morphology of specimens after uniaxial tensile testing as a function of *Ti–Al–Nb–(Zr, Mo)–Si* alloy *GTAW* mode

Conclusion

The effect of *GTAW* modes on the quality of welded joints made of the *Ti_2AlNb*-based alloy *Ti–Al–Nb–(Zr, Mo)–Si* alloy is studied. Based on the results obtained in this work, the following conclusions are drawn:

– A defect-free weld is formed in welding modes at direct and pulsed currents in the range of 80–115 A and with a gas flow rate of 12–15 L/min. At lower welding currents, incomplete penetration (lack of fusion) was detected, while at higher currents, burn-through occurred.

– The welds, depending on the welding modes, have the following microstructure: elongated, large dendrites with a size of 0.23–1.39 mm in the center of the weld; and globular β-grains with a size of 130–190 μm in the root area of the weld. The main volume of the liquid pool is concentrated near the impact of the welding arc. Therefore, columnar dendrites are formed in the central and upper part of the weld, where the maximum heat removal occurs.

– Mechanical testing of *Ti–Al–Nb–(Zr, Mo)–Si* alloy welded joints showed a high strength level of ≈ 90 % of the base metal strength when using the pulsed welding mode (σ_u = 1100 MPa, δ = 1.1 %, 340–380 HV0.2) and not less than 80 % when using direct current modes (σ_u = 1070 MPa, δ = 1.49 %, 335–390 HV0.2).

References

1. Zhao Q., Sun Q., Xin S., Chen Y., Wu C., Wang H., Xu J., Wan M., Zeng W., Zhao Y. High-strength titanium alloys for aerospace engineering applications: a review on melting-forging process. *Materials Science and Engineering: A*, 2022, vol. 845, p. 143260. DOI: 10.1016/j.msea.2022.143260.

2. Marin E., Lanzutti A. Biomedical applications of titanium alloys: a comprehensive review. *Materials (Basel)*, 2024, vol. 17 (2), p. 114. DOI: 10.3390/ma17010114.

3. Ezugwu E.O., Wang Z.M. Titanium alloys and their machinability – a review. *Journal of Materials Processing Technology*, 1997, vol. 68 (3), pp. 262–274. DOI: 10.1016/S0924-0136(96)00030-1.

4. Pasang T., Tao Y., Azizi M., Kamiya O., Mizutani M., Misiolek W. Welding of titanium alloys. *MATEC Web of Conferences*, 2017, vol. 123, pp. 1–8. DOI: 10.1051/matecconf/201712300001.

5. Veiga C., Davim J.P., Loureiro A. Properties and applications of titanium alloys: a brief review. *Reviews on Advanced Materials Science*, 2012, vol. 32 (2), pp. 133–148.

6. Kim Y.-W., Dimiduk D.M. Progress in the understanding of gamma titanium aluminides. *JOM*, 1991, vol. 43, pp. 40–47.

7. Shagiev M.R., Galeyev R.M., Valiakhmetov O.R. Ti_2AlNb-based intermetallic alloys and composites. *Materials Physics and Mechanics*, 2017, vol. 33 (1), pp. 12–18. DOI: 10.18720/MPM.3312017_2.

8. Nandy T.K., Banerjee D. Creep of the orthorhombic phase based on the intermetallic Ti_2AlNb. *Intermetallics*, 2000, vol. 8 (8), pp. 915–928. DOI: 10.1016/S0966-9795(00)00059-5.

9. Dadé M., Esin V.A., Nazé L., Sallot P. Short- and long-term oxidation behaviour of an advanced Ti2AlNb alloy. *Corrosion Science*, 2019, vol. 148, pp. 379–387. DOI: 10.1016/j.corsci.2018.11.036.

10. Xu J., He L., Su H., Zhang L. Tool wear investigation in high-pressure jet coolant assisted machining Ti_2AlNb intermetallic alloys based on FEM. *International Journal of Lightweight Materials and Manufacture*, 2018, vol. 1 (4), pp. 219–228. DOI: 10.1016/j.ijlmm.2018.08.007.

11. Chen W., Li J.W., Xu L., Lu B. Development of Ti2AlNb alloys: opportunities and challenges. *AM&P Technical Articles*, 2014, vol. 172 (5), pp. 23–27. DOI: 10.31399/asm.amp.2014-05.p023.

12. Panov D.O., Naumov S.V., Sokolovsky V.S., Volokitina E.I., Kashaev N., Ventzke V., Dinse R., Riekehr S., Povolyaeva E.A., Alekseev E.B., Nochovnaya N.A., Zherebtsov S.V., Salishchev G.A. Cracking of Ti_2AlNb-based alloy after laser beam welding. *IOP Conference Series: Materials Science and Engineering*, 2021, vol. 1014, p. 012035. DOI: 10.1088/1757-899X/1014/1/012035.

13. Li Y.-J., Wu Ai-P., Li Q., Zhao Y., Zhu R.-C., Wang G.-Q. Mechanism of reheat cracking in electron beam welded Ti_2AlNb alloys. *Transactions of Nonferrous Metals Society of China*, 2019, vol. 29 (9), pp. 1873–1881. DOI: 10.1016/S1003-6326(19)65095-8.

14. Cai D., Chen J., Mao X., Hao C. Reheat cracking in Ti_2AlNb alloy resistance spot weldments. *Intermetallics*, 2013, vol. 38, pp. 63–69. DOI: 10.1016/j.intermet.2013.02.013.

15. Li Y., Zhao Y., Li Q., Wu A., Zhu R., Wang G. Effects of welding condition on weld shape and distortion in electron beam welded Ti2AlNb alloy joints. *Materials & Design*, 2017, vol. 114, pp. 226–233. DOI: 10.1016/j.matdes.2016.11.083.

16. Shao L., Cui E. Joining of Ti-22Al-25Nb alloy using different welding methods. *Materials China*, 2019, vol. 38 (3), pp. 286–290. DOI: 10.7502/j.issn.1674-3962.2019.03.11.

17. Panov D., Naumov S., Stepanov N., Sokolovsky V., Volokitina E., Kashaev N., Ventzke V., Dinse R., Riekehr S., Povolyaeva E., Nochovnaya N., Alekseev E., Zherebtsov S., Salishchev G. Effect of pre-heating and post-weld heat treatment on structure and mechanical properties of laser beam-welded Ti_2AlNb-based joints. *Intermetallics*, 2022, vol. 143, p. 107466. DOI: 10.1016/j.intermet.2022.107466.

18. Zou J., Li H. Review on weldability of Ti_2AlNb-based alloy. *Materials China*, 2019, vol. 38 (7), pp. 710–716. DOI: 10.7502/j.issn.1674-3962.201803012.

19. Liu X., Wu S., Ji Y., Shao L., Zhao H., Wan X. Ultrasonic frequency pulse tungsten inert gas welding of Ti_2AlNb-based alloy. *Xiyou Jinshu / Chinese Journal of Rare Metals*, 2014, vol. 38 (4), pp. 541–547. DOI: 10.13373/j.cnki.cjrm.2014.04.001.

20. Lu B., Yin J., Wang Y., Yang R. Gas tungsten arc welding of Ti_2AlNb based alloy sheet. *Ti-2011: Proceedings of the 12th World Conference on Titanium.* Beijing, 2012, vol. 1, pp. 816–818.

21. Kuang Y., Hu J., Su W., Zhu Z., Liao H., Wang Z. Elimination of pores and microstructural characterization in Ti-6Al-4V alloy welds using fast-frequency double pulse TIG welding. *Materials Today Communications*, 2024, vol. 41, p. 110516. DOI: 10.1016/j.mtcomm.2024.110516.

22. Wang Z., Jiang D., Wu J., Xu M. A review on high-frequency pulsed arc welding. *Journal of Manufacturing Processes*, 2020, vol. 60, pp. 503–519. DOI: 10.1016/j.jmapro.2020.10.054.

23. Karpagaraj A., Siva Shanmugam N., Sankaranarayanasamy K. Some studies on mechanical properties and microstructural characterization of automated TIG welding of thin commercially pure titanium sheets. *Materials Science and Engineering: A*, 2015, vol. 640, pp. 180–189. DOI: 10.1016/j.msea.2015.05.056.

24. Naumov S.V., Panov D.O., Chernichenko R.S., Sokolovsky V.S., Volokitina E.I., Stepanov N.D., Zherebtsov S.V., Alekseev E.B., Nochovnaya N.A., Salishchev G.A. Structure and mechanical properties of welded joints from alloy based on VTI-4 orthorhombic titanium aluminide produced by pulse laser welding. *Izvestiya. Non-Ferrous Metallurgy*, 2023, vol. 29 (2), pp. 57–73. DOI: 10.17073/0021-3438-2023-2-57-73.

25. Kuang Y., Jia J., Zhu Z., Gui Z., Tian J., Wang Z. Study on arc shape, weldment microstructure, and mechanical properties of Ti-6Al-4V welded by FFDP TIG waveform. *The International Journal of Advanced Manufacturing Technology*, 2024, vol. 130, pp. 5269–5284. DOI: 10.1007/s00170-024-13067-z.

Conflicts of Interest

The authors declare no conflict of interest.